RESEARCH ARTICLE

Check for updates

Catalytically active Rh species stabilized by zirconium and hafnium on zeolites†

Yue Song,[a] Tianjun Zhang,[a] Risheng Bai, [ID] *[a] Yida Zhou,[a] Lin Li,[b] Yongcun Zou[a] and Jihong Yu [ID] *[a,c]

Supported subnanometric metal species and metal nanoparticles, prepared through the impregnation method, are widely used in industrial catalysis, but suffer from poor stability of the metal species to sintering at high reaction temperatures. Here, we report that hafnium (Hf) could stabilize rhodium (Rh) metal species supported on zeolites by forming Rh–[O]$_x$–Hf species to resist sintering in an oxidizing or reducing atmosphere at high temperatures (600–700 °C). The resulting RhHf/S-1 is highly efficient in generating H$_2$ from the hydrolysis of ammonia borane (AB), exhibiting a turnover frequency (TOF) of 363 mol$_{H_2}$ mol$_{Rh}^{-1}$ min^{-1} at 25 °C, which is more than 3-fold improvement over that of Hf-free Rh/S-1 (119 mol$_{H_2}$ mol$_{Rh}^{-1}$ min^{-1}). The catalyst also shows superior catalytic activity in the cascade reactions of AB hydrolysis and the hydrogenation of various nitroarenes. Besides the Hf atoms, zirconium (Zr) atoms can also prevent the sintering of precious metal atoms. This sinter resistant strategy can also be extended to platinum (Pt) and ruthenium (Ru) atoms and other supports such as commercial SiO$_2$. This work provides a facile strategy for dispersing and stabilizing precious metal clusters with Zr and Hf additives by a simple impregnation method which will be important for many catalytic processes.

1. Introduction

Supported catalytically active precious metal species, including isolated metal sites, clusters, and nanoparticles, have been widely used in producing clean fuels, chemicals, pharmaceuticals, *etc.*[1–5] The size of the metal species has a great influence on their specific surface area, the number of active sites, their electronic structures, the interaction strength with the support, and thus their catalytic performances.[6–8] However, the sintering of the metal species is an undesirable phenomenon that is involved in catalytic reactions (especially at high temperatures), and results in severe catalyst deactivation. Coalescence and Ostwald ripening are two pathways of metal sintering, which are thermodynamically driven by reducing the chemical potential of the surface atoms.[9–12] Improving chemical bond strength at the metal–support interface can delay the sintering process to a certain extent. This can be achieved by selectively fixing the metal substance on a specific surface of the oxide or coating the metal substance with an oxide shell.[13] However, this kind of catalyst usually requires reducible oxide supports (*e.g.*, CeO$_2$, Co$_3$O$_4$, and FeO$_x$), which exhibit abundant surface oxygen vacancies and can form "strong metal–support interactions",[14–18] while excluding the irreducible commercial oxides (SiO$_2$ and Al$_2$O$_3$), due to the poor reducibility and over-stable surface composition.[19–21] The difficulty in properly matching different metals and different oxides limits the further generality of this method. Physical confinement is another effective method for restraining the metal sintering, especially at temperatures beyond the Tamman temperature of the metal.[3,10] Porous matrices, such as zeolites, MOFs, *etc.*, have been widely investigated as protective matrices, and could not only confine the metal species from sintering but also impede the atom detachment from the support by passivating the susceptible sintering sites.[22–27] However, the narrow opening of the micropores limiting the access of large molecules to the metal species that are confined in the zeolite channels or cages, and the difficulty in controlling the size of the metal species are two aspects that should be overcome and cannot be ignored.[28,29] Therefore, preparing sinter-resistant supported precious metal catalysts on carriers with open structures, especially the irreducible ones, is challenging.

It has been demonstrated that the presence of secondary elements, such as Zn, Sn, Co, Bi, Na, and K, could substan-

[a] State Key Laboratory of Inorganic Synthesis and Preparative Chemistry, College of Chemistry, Jilin University, Changchun 130012, China. E-mail: rsbai@jlu.edu.cn, Jihong@jlu.edu.cn

[b] Electron Microscopy Center, Jilin University, Changchun 130012, China

[c] International Center of Future Science, Jilin University, Changchun 130012, China. E-mail: jihong@jlu.edu.cn

This journal is © the Partner Organisations 2022

Inorg. Chem. Front., 2022, **9**, 2395–2402 | **2395**

tially modulate the electronic structures of precious metals (*e.g.*, Pt and Au), and thus their catalytic performances.[30–33] Flytzani-Stephanopoulos and co-workers reported that the presence of alkali ions (Na or K) could stabilize the Pt and Au in the Pt–alkali–$O_x(OH)_y$ and Au–$O(OH)_x$–(Na or K)$_y$ ensembles, respectively, even with the irreducible SiO_2 or Al_2O_3 as the supports.[33,34] The existing alkali could stabilize and provide the oxygen-containing species (OH) to the Pt and Au atoms and stabilize the metal atoms in their oxide form, which showed excellent catalytic performances in the low-temperature water–gas shift reaction. Recently, Si and co-workers showed that bismuth (Bi) could act as a dopant to form a platinum-bismuth cluster on silica; the formed partially oxidized Pt–$[O]_x$–Bi structure has been proven to be the active site for a CO oxidation reaction, which could moderate the adsorption toward CO and activate CO molecules through the electron transfer between Pt and CO, thus showing outstanding catalytic performance.[35] However, there is still a lack of studies to extend the above findings to other precious metals, such as rhodium (Rh) and ruthenium (Ru), which might be neither obvious nor anticipated. In this respect, taking advantage of the modulation effect of the secondary element, the sintering of the subnanometric Rh/Ru species or nanoparticles can be alleviated.

In this work, we demonstrate that zirconium (Zr) and hafnium (Hf) can act as a dopant to constrain the sintering of precious metal atoms (Rh, Ru, and Pt) by forming partially oxidized species (for example, Rh–$[O]_x$–Hf). Supported catalysts were prepared with irreducible **MFI** zeolites (pure siliceous silicalite-1 and aluminosilicate ZSM-5) as supports by an incipient wetness impregnation method. The dopant of Hf stabilizes the Rh clusters by forming a Rh–$[O]_x$–Hf structure on the surface of the Rh cluster, which dramatically limited the migration of Rh atoms or nanoparticles under high temperature conditions. Compared with the Rh/S-1 catalyst that is free from the modification of Hf, the RhHf/S-1 catalyst exhibited extraordinary sinter resistance in oxide or redox atmospheres and demonstrated superior catalytic performance in the ammonia borane (AB, NH_3BH_3) hydrolysis as well as the corresponding cascade nitroarene hydrogenation reactions.

2. Results and discussion

Scheme 1a and b depict the schematic illustration of the synthesis process of ultrasmall noble metal clusters (represented by Rh, RhHf, and RhZr) supported on **MFI** zeolites through an incipient wetness impregnation method. A silicalite-1 (S-1) zeolite support was prepared with tetrapropylammonium hydroxide (TPAOH) as the organic template with a gel composition of $SiO_2 : 0.2$ TPAOH : 35 H_2O under hydrothermal conditions at 170 °C for one day, which displays a coffin-like morphology with a size of ~250 nm (Fig. S1†). Rh, RhHf, and RhZr clusters were immobilized on the S-1 support by impregnation with $RhCl_3$ solution or a mixture of $RhCl_3$ and $ZrCl_4/HfCl_4$ solutions in zeolites, followed by reduction in H_2 at 400 °C for
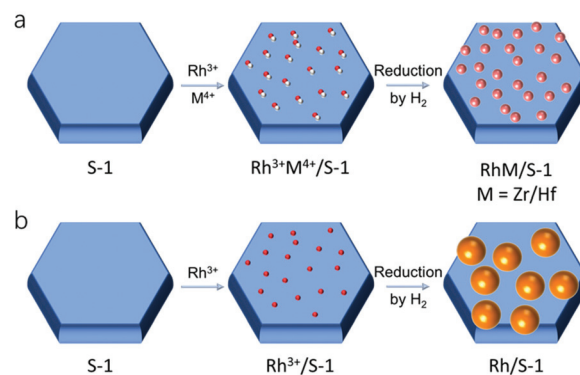

Scheme 1 Schematic illustration of the formation process of (a) RhZr/S-1, RhHf/S-1, and (b) Rh/S-1 zeolite samples through the wetness impregnation method.

2 h. The prepared samples are named Rh/S-1, RhZr/S-1, and RhHf/S-1, respectively. The powder X-ray diffraction (XRD) patterns (Fig. S2†) and N_2 adsorption–desorption isotherms (Fig. S3 and Table S1†) of all the Rh supported zeolite samples exhibit characteristic diffraction patterns of **MFI** topology and high crystallinity. Due to the ultrasmall sizes, low loading amounts, and relatively uniform dispersions, no typical diffraction peaks of metallic Rh in these Rh-loaded samples were detected.

As measured by the inductively coupled plasma-optical emission spectroscopy (ICP-OES), Rh loading amounts are 0.45 and 0.32 wt% for RhZr/S-1 (Zr: 0.68 wt%) and RhHf/S-1 (Hf: 1.43 wt%), respectively, higher than that of Rh/S-1 (Rh: 0.12 wt%) (Table S1†). Notably, before the high-temperature reduction treatment, the content of Rh in both RhHf/S-1 and Rh/S-1 is 0.49 wt% (similar to the theoretical value of 0.50 wt%), while after the high-temperature treatment process, the RhHf/S-1 sample exhibits higher Rh loading amounts than Rh/S-1 (0.32 *vs.* 0.12 wt%), indicating that the presence of Hf could facilitate the immobilization of Rh on S-1 zeolite support and suppress the loss of Rh during high temperature treatment. Significantly, the presence of Zr/Hf within the impregnation solution could dramatically influence the size of the Rh species. Scanning transmission electron microscopy (STEM) and transmission electron microscopy (TEM) images of the Rh/S-1 zeolite sample show that the supported Rh nanoparticles are mainly in the range of 2–6 nm (Fig. 1a–d and Fig. S4†), while Rh clusters of 1.6–1.7 nm with narrow size distribution are detected in RhHf/S-1 and RhZr/S-1 zeolite samples (Fig. 1e–l and Fig. S5, S6†). The corresponding energy dispersive spectroscopy (EDS) mappings for Rh, Hf, Zr, and Si of RhHf/S-1 or RhZr/S-1 zeolite samples reveal that the Rh and Hf/Zr elements are uniformly distributed throughout the S-1 zeolite support without evident separation (Fig. S7 and S8†). The above results clearly indicate that Zr or Hf species could prevent the sintering of Rh metallic particles on the **MFI** zeolites.

^{1}H and ^{29}Si MAS NMR spectroscopy were applied to investigate the Si and Si–OH species of the prepared Rh-supported zeolite samples. As shown in Fig. 2a, the ^{29}Si MAS NMR
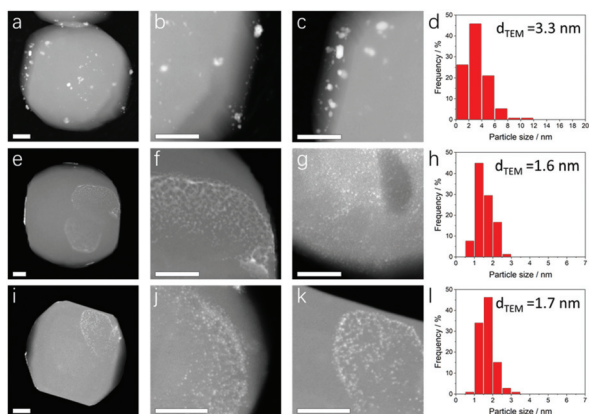
Fig. 1 STEM images and the corresponding size distributions of Rh particles of different Rh−zeolite samples after reduction with H_2 at 400 °C. (a−d) Rh/S-1, (e−h) RhHf/S-1, and (i−l) RhZr/S-1. Scale bars, 50 nm. The average particle size of the metal clusters is calculated according to the formula $d_{TEM} = \sum n_i d_i^3 / \sum n_i d_i^2$, where n_i represents the particle number with a size of d_i.
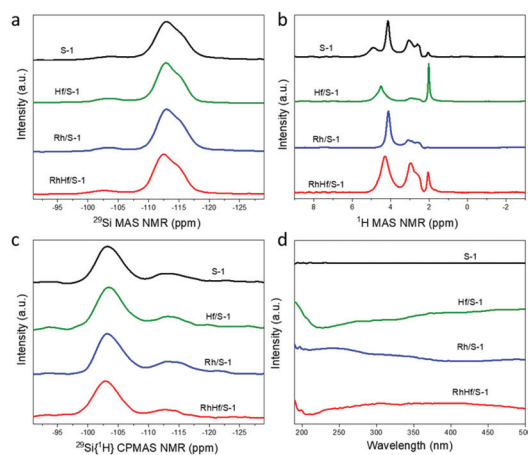
Fig. 2 (a) ^{29}Si MAS NMR, (b) ^{1}H MAS NMR, (c) ^{1}H-^{29}Si CP-MAS NMR, and (d) UV-vis spectra of the impregnated S-1 zeolite samples.

spectra reveal that all these silicalite-1 zeolite samples exhibit predominant signal peaks at −110 to −115 ppm, which are ascribed to the Si(4Si) species, suggesting that the introduction of Hf and/or Rh species does not disturb the structural integrity of the zeolite framework. The ^{1}H MAS NMR spectroscopy was applied to study the silanol groups in the prepared samples (Fig. 2b). The peaks at the chemical shifts of 2.0 ppm, 2.6 ppm, and 3.0–4.3 ppm are ascribed to the isolated Si–OH, geminal or vicinal Si–OH, and H-bonded silanol groups, respectively.[36–38] As can be seen, the immobilization of Rh and Hf species could lead to the decrease of the silanol groups, suggesting that the silanol groups take the responsibility to immobilize the Rh and/or Hf species. ^{1}H-^{29}Si CP-MAS NMR spectra further reveal the existence of abundant silanol groups in zeolite samples, even after the immobilization of the Rh and/or Hf species (Fig. 2c). UV-visible (UV-vis) spectroscopy
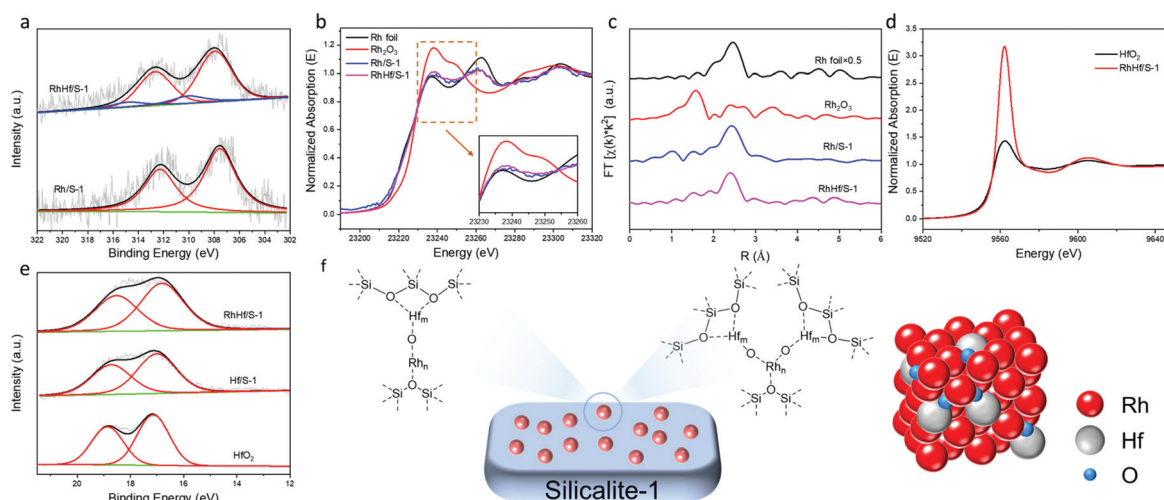
indicates that Hf/S-1 exhibits absorption bands at 200 nm and 220–260 nm, which are ascribed to the isolated Hf(IV) and HfO_x clusters, respectively.[39–41] The Rh/S-1 sample shows absorption bands at 260 nm and 320 nm, ascribed to the Rh–O charge transfer and the $^1A_{1g} \rightarrow {}^1T_{1g}$ transition, respectively.[42] Thus, the absorption bands of RhHf/S-1 at 200 nm and 260 nm can be the superposition of two different bands (Fig. 2d). We infer that the oxygen from the Si–OH groups may form covalent bonds with Rh^{3+} and Hf^{4+} ions during the high temperature treatment under a H_2 atmosphere at 400 °C, resulting in the formation of RhO_x and HfO_x.

To identify the electronic states of the supported metal species, X-ray photoelectron spectroscopy (XPS) measurements were performed. The peaks at 307.5 and 312.3 eV corresponding to the Rh $3d_{5/2}$ and Rh $3d_{3/2}$ of Rh^0 can be observed in Rh/S-1 (Fig. 3a).[43] Notably, the corresponding two peaks marginally shift to higher binding energies of 307.9 and 312.7 eV in the RhHf/S-1 sample, suggesting that the Rh species in RhHf/S-1 exhibits a higher valence state than that in the Rh/S-1 sample, and the $Rh^{\delta+}$ species accounts for 16% of the total Rh amount (Table S2†).

The X-ray absorption fine structure (XAFS) technique was used to identify the local structure of Rh clusters in Rh/S-1 and Hf-promoted RhHf/S-1 samples. In comparison to Rh foil, the slightly higher white-line intensity in the Rh K-edge X-ray absorption near-edge structure (XANES) spectra of the Rh/S-1 and RhHf/S-1 samples indicates the presence of the oxidized state of Rh in these samples (Fig. 3b). The enhanced valence state of Rh may be ascribed to the formed ultrasmall clusters and the interaction between the Rh and the skeleton oxygen atoms of the silicalite-1 support. Moreover, in the case of RhHf/S-1, the enhancement of the valence state of Rh may be ascribed to the interaction between Rh with Hf and/or Hf oxide species grafted on the S-1 support through the abundant oxygen around the Rh atom. The extended X-ray absorption fine structure (EXAFS) fitting results show the existence of a Rh–O shell ($R \approx 2.04$ Å, CN ≈ 1.7) and a Rh–Rh shell ($R \approx 2.69$ Å, CN ≈ 6.3) in the Rh/S-1 zeolite sample; while in the RhHf/S-1 zeolite sample, besides the major Rh–O shell ($R \approx 2.02$ Å, CN ≈ 1.5) and the Rh–Rh shell ($R \approx 2.67$ Å, CN ≈ 4.4), an apparent Rh–O–Hf component ($R \approx 3.54$ Å, CN ≈ 1.6) is also present, indicating the existence of the Rh–[O]$_x$–Hf structure. The lower coordination number of Rh–Rh in the RhHf/S-1 sample suggests that the Rh clusters in the sample are smaller than that in Rh/S-1, which is in accordance with the TEM results. Besides, the distance between the Rh–Rh atoms in the RhHf/S-1 sample is slightly shorter than that in the Rh/S-1 sample (2.67 Å *vs.* 2.69 Å), implying that the formation of Rh–O–Hf species leads to the lattice contraction of the Rh clusters,[44] which might be due to the strong interactions in the Rh–O–Hf species (Fig. 3c, Fig. S9, and Table S3†).

Furthermore, the nature of the Hf species in the RhHf/S-1 sample was also investigated through Hf L_3-edge XAS. XANES analysis shows that the Hf species are in the oxidation state for the RhHf/S-1 sample (Fig. 3d). We also studied the XPS spectra of Hf for HfO_2, Hf/S-1, and RhHf/S-1 samples (Fig. 3e). The Hf/

This journal is © the Partner Organisations 2022

Inorg. Chem. Front., 2022, **9**, 2395–2402 | **2397**

Fig. 3 (a) Rh 3d XPS spectra, (b) Rh K-edge XANES spectra, and (c) Fourier transform of k^2-weighted spectra of Rh/S-1 and RhHf/S-1 samples; (d) Hf L_3-edge XANES profile of the RhHf/S-1 sample; (e) Hf 4f XPS spectra, and (f) schematic illustration of Rh–Hf clusters.

S-1 sample shows the Hf $4f_{7/2}$ and Hf $4f_{5/2}$ peaks at 17.0 and 18.7 eV, which are close to the peaks in HfO_2 (17.1 and 18.8 eV), indicating the oxidation state of the Hf species in the sample. In addition, in the RhHf/S-1 sample, the Hf $4f_{7/2}$ and Hf $4f_{5/2}$ peaks shift to lower binding energies (16.8 and 18.5 eV), suggesting that the electrons may transfer from Rh to Hf in the RhHf/S-1 sample. Based on the above-mentioned results, we present a schematic illustration of Rh–Hf clusters supported on the S-1 zeolite, mainly demonstrating the presence of Rh–$[O]_x$–Hf species and the interaction between Rh and Hf (Fig. 3f).

The thermal stability of the Rh/S-1 and RhHf/S-1 samples was investigated through high temperature treatment under a H_2–O_2 cycle atmosphere at 600 °C. After five cycles of reduction–oxidation treatment at 600 °C, the size of bimetallic RhHf clusters in RhHf/S-1 increased by 12.5% from 1.6 nm to 1.8 nm; while the Rh nanoparticles in Rh/S-1 increased by 30% (from 3.3 nm to 4.3 nm) (Fig. S10 and S11†). To investigate the hydrothermal stability of the prepared Rh-supported samples, steam aging treatment was performed at 700 °C with N_2 flow containing 10 vol% of water vapor for 1 hour. The average metal size of the RhHf clusters in RhHf/S-1 increased from 1.6 to 1.7 nm (Fig. S12†). In contrast, the Rh nanoparticles in the Rh/S-1 sample underwent severe aggregation, with the particle size increasing from 3.3 to 5.3 nm (Fig. S13†). The XRD patterns indicate that the crystallinity of the zeolite supports remains intact after the high temperature treatment (Fig. S14†). The above results further indicate that the presence of Hf could significantly inhibit metal sintering under high temperature conditions by forming a Rh–$[O]_x$–Hf structure.

To demonstrate the generality of this method in preparing sinter-resistant catalysts, we also immobilized Rh species on NaOH-treated SiO_2 by the incipient wetness impregnation method, followed by reduction in H_2 at 400 °C. The obtained RhHf/SiO_2 sample exhibits smaller Rh species than the Rh/

SiO_2 sample (1.6 vs. 3.8 nm) (Fig. S15 and S16†). In addition, we also prepared Pt/S-1, Ru/S-1, PtHf/S-1, and RuHf/S-1 samples by the same impregnation method and high temperature treatment. Fig. S17–S20† demonstrate that the presence of Hf could dramatically reduce the noble metal particle size (4.7 nm and 1.8 nm for Pt/S-1 and PtHf/S-1, respectively; 4.5 nm and 1.9 nm for Ru/S-1 and RuHf/S-1, respectively). The above results demonstrate the universality of this preparation method in preventing noble metal sintering under high temperature conditions.
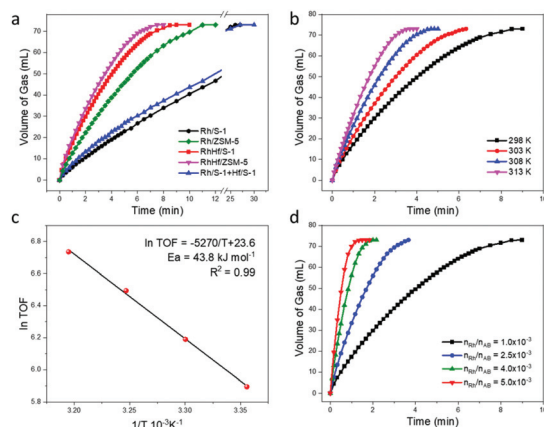
Catalytic experiments

We demonstrate the catalytic performance of the Rh-supported catalysts in the hydrolysis of AB. The AB hydrolysis follows the following equation:

$$NH_3BH_3 + 2H_2O \xrightarrow{\text{Catalysts}} NH_4^+ + BO_2^- + 3H_2 \uparrow$$
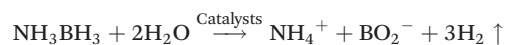
As shown in Fig. 4a, the RhHf/S-1 catalyst exhibits a higher hydrogen generation rate than the Rh/S-1 catalyst, affording a TOF of 363 mol_{H_2} mol_{Rh}^{-1} min^{-1} at 25 °C, which is 3-fold higher than that of the Hf-free Rh/S-1 catalyst (119 mol_{H_2} mol_{Rh}^{-1} min^{-1}).

The products in the gas or liquid phase were analyzed through gas chromatography, ^1H NMR spectroscopy, and ^{11}B NMR spectroscopy (Fig. S21–S23†). Furthermore, the RhHf loaded zeolite catalyst with a larger particle size was prepared by increasing the reduction temperature from 400 °C to 800 °C, and the obtained sample was named RhHf/S-1(800 °C) (Fig. S24†). In comparison to the Rh/S-1 sample (with a Rh particle size of about 3.3 nm) and the RhHf/S-1(800 °C) sample (with a Rh particle size of about 1.8 nm), the RhHf/S-1 catalyst (with a Rh particle size of about 1.6 nm) exhibits higher catalytic activity in the hydrolysis of AB. The TOF values of Rh/S-1, RhHf/S-1(800 °C), and RhHf/S-1 are 119, 238, and 363 mol_{H_2} mol_{Rh}^{-1} min^{-1}, respectively (Fig. 4a and S25†), indicating that

2398 | *Inorg. Chem. Front.*, 2022, **9**, 2395–2402

This journal is © the Partner Organisations 2022

Fig. 4 Hydrolysis reaction activity of ammonia borane (AB). (a) Volume of the H_2 produced from AB hydrolysis *versus* time over Rh/S-1, Rh/ZSM-5, RhHf/S-1, and RhHf/ZSM-5 catalysts; reaction conditions: 25 °C, 1 mol L^{-1} of AB, $n_{Rh}/n_{AB} = 0.001$; (b) activity at various temperatures over the RhHf/S-1 catalyst; (c) Arrhenius plot (ln TOF *versus* 1/*T*) for RhHf/S-1; (d) catalytic activity at various catalyst concentrations over the RhHf/S-1 catalyst at 25 °C.

the reduction of the noble metal particle size could facilitate the hydrolysis of AB. Besides, the Hf/S-1 catalyst exhibits no catalytic activity towards the AB hydrolysis and the physical mixture of Rh/S-1 and Hf/S-1 also shows identical catalytic activity to the monometallic Rh/S-1 catalyst, indicating that the bimetallic synergistic effect between Rh and Hf in the RhHf/S-1 catalyst plays an important role in improving the catalytic activities (Fig. 4a). According to the above experimental results, we conclude that the superior catalytic performance of the RhHf/S-1 zeolite catalyst can be ascribed to the reduced size of Rh clusters and the synergetic effect between Rh and Hf.

The isotopic experiments were carried out using D_2O instead of H_2O as the reactant to gain deeper insight into the mechanism of AB hydrolysis. The ratio of the reaction rate constants for H_2O and D_2O is defined as the kinetic isotope effect (KIE), *i.e.*, KIE = k_{H_2O}/k_{D_2O}. The KIE values of RhHf/S-1 and Rh/S-1 zeolite catalysts are 4.78 and 6.92, respectively (Fig. S26†), suggesting that the activation and cleavage of the O–H bond of the water molecule is the rate-determining step in the reaction of AB hydrolysis, which is consistent with previously published works,[45,46] and the introduction of Hf into the catalyst does not change the catalytic mechanism of AB hydrolysis. Notably, RhHf/S-1 exhibits a lower KIE value than Rh/S-1, showing that the bimetallic synergetic effect between Rh and Hf could facilitate the activation of the water molecule.

It is notable that the catalytic activity towards AB hydrolysis can be improved by introducing Al into the zeolite support. The introduction of Al could bring Brønsted acidic sites into the zeolite support, which could cooperate with the loaded Rh species and activate both water and AB molecules.[29,47,48] Rh/ZSM-5 and RhHf/ZSM-5 were then prepared using commercial ZSM-5 (with Si/Al = 31) as the support. As shown in Fig. S27 and S28,† the existence of Hf could dramatically hinder the

sintering of the Rh clusters, and the particle size is about 1.6 nm for RhHf/ZSM-5 and 3.0 nm for the Rh/ZSM-5 sample. In comparison to the pure siliceous RhHf/S-1, RhHf/ZSM-5 demonstrates higher catalytic efficiency in the AB hydrolysis, verifying the synergetic effect between the Brønsted acidic sites and the noble metal clusters. The TOF value of RhHf/ZSM-5 increased to 412 mol_{H_2} mol_{Rh}^{-1} min^{-1} at 25 °C (Fig. 4a).

In addition, detailed effects of the reaction conditions, including the concentration of Rh species and the reaction temperature, were also investigated with RhHf/S-1 as a typical catalyst. Fig. 4b shows the hydrolysis of AB at different reaction temperatures over the RhHf/S-1 catalyst, and the TOF value reaches up to 841 mol_{H_2} mol_{Rh}^{-1} min^{-1} at 40 °C. The apparent activation energy of RhHf/S-1 is 43.8 kJ mol^{-1}, calculated according to the Arrhenius plot (Fig. 4c), dramatically lower than that of the Rh/S-1 sample (50.3 kJ mol^{-1}) (Fig. S29†). Fig. 4d shows that the reaction rate increases with the increase of the Rh catalyst concentration. The linear logarithm diagram of the apparent reaction rate and the catalyst concentration shows that when the concentration of AB is fixed, the reaction rate has a first-order correlation with the concentration of the catalyst (Fig. S30†).

The catalytic activity of Rh-supported catalysts for tandem reactions that involved the coupling of AB hydrolysis with nitroarene hydrogenation was also investigated (Table 1). The nitrobenzene could be completely reduced to the corres-

Table 1 Conversion and selectivity for the tandem hydrogenation of various nitroarenes by coupling with AB hydrolysis[a]

Entry	Catalyst	Substrate	Product	Time/ min	Con./ %	Sel./ %
1	RhHf/S-1	NO_2	NH_2	7	>99	>99
2	Rh/S-1			20	>99	>99
3	RhHf/S-1	NO_2 CH_3	NH_2 CH_3	15	>99	>99
4	RhHf/S-1	NO_2	NH_2	15	>99	>99
5	RhHf/S-1			7	>99	>99
6	RhHf/S-1			15	>99	>99
7	RhHf/S-1	NO_2 F	NH_2 F	15	>99	>99
8	RhHf/S-1	NO_2 Cl	NH_2 Cl	15	>99	>99
9	RhHf/S-1	NO_2 Br	NH_2 Br	15	>99	>99
10	RhHf/S-1	NO_2	NH_2	15	>99	>99
11	RhHf/S-1[b]	NO_2	NH_2	7	>99	>99

[a] Reaction conditions: 1 mmol of NH_3BH_3, 0.1 mmol of nitro compound, the Rh/nitroarene ratio is 0.019, 8 mL of MeOH, 12 mL of H_2O, 25 °C. [b] RhHf/S-1 catalyst after five recycling tests in the tandem hydrogenation of nitrobenzene.

This journal is © the Partner Organisations 2022

Inorg. Chem. Front., 2022, **9**, 2395–2402 | **2399**

ponding aniline within 7 minutes over the RhHf/S-1 catalyst and with a selectivity higher than 99%, showing superior catalytic activity to Rh/S-1 (>99% conversion in 20 minutes). The superior catalytic activity of RhHf/S-1 can be attributed to the reduced size of Rh clusters and the special structure of the formed Rh–[O]$_x$–Hf species. Moreover, besides the nitrobenzene, some other nitroarenes, even in bulky size, such as 1-methyl-2-nitrobenzene, 1-methyl-4-nitrobenzene, 1,2-dimethyl-4-nitrobenzene, 1,3-dimethyl-5-nitrobenzene, 1-fluoro-4-nitrobenzene, 1-chloro-4-nitrobenzene, 1-bromo-4-nitrobenzene, and 1-nitronaphthalene can also be effectively converted into the corresponding amines with a selectivity higher than 99% (Table 1).

The recycling tests of AB hydrolysis and tandem hydrogenation of nitrobenzene over the RhHf/S-1 catalyst were carried out. After five recycling tests of AB hydrolysis, the catalytic activity of the RhHf/S-1 catalyst slightly decreases (Fig. S31†), which can be ascribed to the increased RhHf nanoparticle size (from 1.6 to 1.9 nm, Fig. 1e–h and S32†). Notably, in the durability test of the tandem hydrogenation of nitrobenzene over the RhHf/S-1 catalyst, a conversion of 99% and a selectivity exceeding 99% can also be achieved even in the fifth recycling reaction test (Table 1, entry 11).

3. Conclusion

In summary, we have developed a Zr/Hf-assisted incipient wetness impregnation synthesis method for the preparation of sintering-resistant noble metal (such as Rh, Ru, and Pt) catalysts over zeolite or SiO$_2$ support. In comparison to the Hf-free sample, the prepared RhHf/S-1 catalyst exhibits excellent sintering resistance even in a redox atmosphere because of the formation of Rh–[O]$_x$–Hf, as revealed by the XAS analyses, and shows superior catalytic performance in H$_2$ generation *via* the hydrolysis of ammonia borane, affording a TOF value of 363 mol$_{H_2}$ mol$_{Rh}^{-1}$ min^{-1} at 25 °C. The RhHf/S-1 catalyst also shows excellent efficiency in tandem ammonia borane hydrolysis and hydrogenation of nitroarenes. Most significantly, Hf-assisted samples demonstrate excellent resistance of the metals (such as Rh, Ru, and Pt) to sintering, even under harsh conditions, which can be anticipated to show excellent catalytic activity in other important catalytic processes. Since this method is universal in suppressing the sintering of noble metals on the irreducible zeolite support, we expect that this method can be extended to other metals and supports.

Conflicts of interest

The authors declare no competing financial interest.

Acknowledgements

References

1 L. Liu and A. Corma, Metal catalysts for heterogeneous catalysis: From single atoms to nanoclusters and nanoparticles, *Chem. Rev.*, 2018, **118**, 4981–5079.

2 N. Wang, Q. Sun and J. Yu, Ultrasmall metal nanoparticles confined within crystalline nanoporous materials: A fascinating class of nanocatalysts, *Adv. Mater.*, 2019, **31**, 1803966.

3 L. Wang, L. Wang, X. Meng and F.-S. Xiao, New strategies for the preparation of sinter-resistant metal-nanoparticle-based catalysts, *Adv. Mater.*, 2019, **31**, 1901905.

4 J. Zhang, L. Wang, B. Zhang, H. Zhao, U. Kolb, Y. Zhu, L. Liu, Y. Han, G. Wang, C. Wang, D. S. Su, B. C. Gates and F.-S. Xiao, Sinter-resistant metal nanoparticle catalysts achieved by immobilization within zeolite crystals via seed-directed growth, *Nat. Catal.*, 2018, **1**, 540–546.

5 X. Yang, J.-K. Sun, M. Kitta, H. Pang and Q. Xu, Encapsulating highly catalytically active metal nanoclusters inside porous organic cages, *Nat. Catal.*, 2018, **1**, 214–220.

6 J. Zhu, M.-L. Yang, Y. Yu, Y.-A. Zhu, Z.-J. Sui, X.-G. Zhou, A. Holmen and D. Chen, Size-dependent reaction mechanism and kinetics for propane dehydrogenation over Pt catalysts, *ACS Catal.*, 2015, **5**, 6310–6319.

7 C. T. Campbell, S. C. Parker and D. E. Starr, The effect of size-dependent nanoparticle energetics on catalyst sintering, *Science*, 2002, **298**, 811–814.

8 R. J. White, R. Luque, V. L. Budarin, J. H. Clark and D. J. Macquarrie, Supported metal nanoparticles on porous materials. Methods and applications, *Chem. Soc. Rev.*, 2009, **38**, 481–494.

9 W. Yuan, D. Zhang, Y. Ou, K. Fang, B. Zhu, H. Yang, T. W. Hansen, J. B. Wagner, Z. Zhang, Y. Gao and Y. Wang, Direct in situ TEM visualization and insight into the facet-dependent sintering behaviors of gold on TiO$_2$, *Angew. Chem., Int. Ed.*, 2018, **57**, 16827–16831.

10 T. W. Hansen, A. T. DeLaRiva, S. R. Challa and A. K. Datye, Sintering of catalytic nanoparticles: Particle migration or Ostwald ripening?, *Acc. Chem. Res.*, 2013, **46**, 1720–1730.

11 S. R. Challa, A. T. Delariva, T. W. Hansen, S. Helveg, J. Sehested, P. L. Hansen, F. Garzon and A. K. Datye, Relating rates of catalyst sintering to the disappearance of individual nanoparticles during Ostwald ripening, *J. Am. Chem. Soc.*, 2011, **133**, 20672–20675.

12 K.-J. Hu, S. R. Plant, P. R. Ellis, C. M. Brown, P. T. Bishop and R. E. Palmer, Atomic resolution observation of a size-dependent change in the ripening modes of mass-selected Au nanoclusters involved in CO oxidation, *J. Am. Chem. Soc.*, 2015, **137**, 15161–15168.

13 T. W. van Deelen, C. Hernández Mejía and K. P. de Jong, Control of metal-support interactions in heterogeneous cat-

alysts to enhance activity and selectivity, *Nat. Catal.*, 2019, **2**, 955–970.

14 L. Nie, D. Mei, H. Xiong, B. Peng, Z. Ren, X. I. P. Hernandez, A. DeLaRiva, M. Wang, M. H. Engelhard, L. Kovarik, A. K. Datye and Y. Wang, Activation of surface lattice oxygen in single-atom Pt/CeO$_2$ for low-temperature CO oxidation, *Science*, 2017, **358**, 1419–1423.

15 K. An, S. Alayoglu, N. Musselwhite, S. Plamthottam, G. Melaet, A. E. Lindeman and G. A. Somorjai, Enhanced CO oxidation rates at the interface of mesoporous oxides and Pt nanoparticles, *J. Am. Chem. Soc.*, 2013, **135**, 16689–16696.

16 B. Qiao, A. Wang, X. Yang, L. F. Allard, Z. Jiang, Y. Cui, J. Liu, J. Li and T. Zhang, Single-atom catalysis of CO oxidation using Pt$_1$/FeO$_x$, *Nat. Chem.*, 2011, **3**, 634–641.

17 A. Chen, X. Yu, Y. Zhou, S. Miao, Y. Li, S. Kuld, J. Sehested, J. Liu, T. Aoki, S. Hong, M. F. Camellone, S. Fabris, J. Ning, C. Jin, C. Yang, A. Nefedov, C. Wöll, Y. Wang and W. Shen, Structure of the catalytically active copper–ceria interfacial perimeter, *Nat. Catal.*, 2019, **2**, 334–341.

18 B. Lin, Y. Wu, B. Fang, C. Li, J. Ni, X. Wang, J. Lin and L. Jiang, Ru surface density effect on ammonia synthesis activity and hydrogen poisoning of ceria-supported Ru catalysts, *Chin. J. Catal.*, 2021, **42**, 1712–1723.

19 N. Almana, S. P. Phivilay, P. Laveille, M. N. Hedhili, P. Fornasiero, K. Takanabe and J.-M. Basset, Design of a core–shell Pt–SiO$_2$ catalyst in a reverse microemulsion system: Distinctive kinetics on CO oxidation at low temperature, *J. Catal.*, 2016, **340**, 368–375.

20 M. Haneda, T. Watanabe, N. Kamiuchi and M. Ozawa, Effect of platinum dispersion on the catalytic activity of Pt/Al$_2$O$_3$ for the oxidation of carbon monoxide and propene, *Appl. Catal., B*, 2013, **142–143**, 8–14.

21 M. Boaro, M. Vicario, J. Llorca, C. de Leitenburg, G. Dolcetti and A. Trovarelli, A comparative study of water gas shift reaction over gold and platinum supported on ZrO$_2$ and CeO$_2$–ZrO$_2$, *Appl. Catal., B*, 2009, **88**, 272–282.

22 L. Liu and A. Corma, Confining isolated atoms and clusters in crystalline porous materials for catalysis, *Nat. Rev. Mater.*, 2021, **6**, 244–263.

23 N. Kosinov, C. Liu, E. J. M. Hensen and E. A. Pidko, Engineering of transition metal catalysts confined in zeolites, *Chem. Mater.*, 2018, **30**, 3177–3198.

24 N. Wang, Q. Sun, R. Bai, X. Li, G. Guo and J. Yu, In situ confinement of ultrasmall Pd clusters within nanosized silicalite-1 zeolite for highly efficient catalysis of hydrogen generation, *J. Am. Chem. Soc.*, 2016, **138**, 7484–7487.

25 Y. Chai, W. Dai, G. Wu, N. Guan and L. Li, Confinement in a zeolite and zeolite catalysis, *Acc. Chem. Res.*, 2021, **54**, 2894–2904.

26 L. Jiao, Y. Wang, H.-L. Jiang and Q. Xu, Metal–organic frameworks as platforms for catalytic applications, *Adv. Mater.*, 2018, **30**, 1703663.

27 H. Liu, L. Chen, C.-C. Hou, Y.-S. Wei and Q. Xu, Soluble porous carbon cage-encapsulated highly active metal nanoparticle catalysts, *J. Mater. Chem. A*, 2021, **9**, 13670–13677.

28 W. Xu, L. Li, T. Zhang and J. Yu, Tailoring porosity and titanium species of TS-1 zeolites *via* organic base-assisted sequential post-treatment, *Chem. Res. Chin. Univ.*, 2022, **38**, 50–57.

29 Q. Sun, N. Wang, T. Zhang, R. Bai, A. Mayoral, P. Zhang, Q. Zhang, O. Terasaki and J. Yu, Zeolite-encaged single-atom rhodium catalysts: Highly-efficient hydrogen generation and shape-selective tandem hydrogenation of nitroarenes, *Angew. Chem., Int. Ed.*, 2019, **58**, 18570–18576.

30 Q. Sun, N. Wang, Q. Fan, L. Zeng, A. Mayoral, S. Miao, R. Yang, Z. Jiang, W. Zhou, J. Zhang, T. Zhang, J. Xu, P. Zhang, J. Cheng, D.-C. Yang, R. Jia, L. Li, Q. Zhang, Y. Wang, O. Terasaki and J. Yu, Subnanometer bimetallic platinum–zinc clusters in zeolites for propane dehydrogenation, *Angew. Chem., Int. Ed.*, 2020, **59**, 19450–19459.

31 L. Liu, M. Lopez-Haro, C. W. Lopes, S. Rojas-Buzo, P. Concepcion, R. Manzorro, L. Simonelli, A. Sattler, P. Serna, J. J. Calvino and A. Corma, Structural modulation and direct measurement of subnanometric bimetallic PtSn clusters confined in zeolites, *Nat. Catal.*, 2020, **3**, 628–638.

32 H. Xu, Q. Fu, X. Guo and X. Bao, Architecture of Pt-Co bimetallic catalysts for catalytic CO oxidation, *ChemCatChem*, 2012, **4**, 1645–1652.

33 Y. Zhai, D. Pierre, R. Si, W. Deng, P. Ferrin, A. U. Nilekar, G. Peng, J. A. Herron, D. C. Bell, H. Saltsburg, M. Mavrikakis and M. Flytzani-Stephanopoulos, Alkali-stabilized Pt-OH$_x$ species catalyze low-temperature water-gas shift reactions, *Science*, 2010, **329**, 1633–1636.

34 M. Yang, S. Li, Y. Wang, J. A. Herron, Y. Xu, L. F. Allard, S. Lee, J. Huang, M. Mavrikakis and M. Flytzani-Stephanopoulos, Catalytically active Au-O(OH)$_x$-species stabilized by alkali ions on zeolites and mesoporous oxides, *Science*, 2014, **346**, 1498–1501.

35 B. Nan, Q. Fu, J. Yu, M. Shu, L.-L. Zhou, J. Li, W.-W. Wang, C.-J. Jia, C. Ma, J.-X. Chen, L. Li and R. Si, Unique structure of active platinum-bismuth site for oxidation of carbon monoxide, *Nat. Commun.*, 2021, **12**, 3342.

36 A.-B. Fernández, A. Marinas, T. Blasco, V. Fornés and A. Corma, Insight into the active sites for the Beckmann rearrangement on porous solids by in situ infrared spectroscopy, *J. Catal.*, 2006, **243**, 270–277.

37 G. P. Heitmann, G. Dahlhoff and W. F. Hölderich, Catalytically active sites for the Beckmann rearrangement of cyclohexanone oxime to ε-Caprolactam, *J. Catal.*, 1999, **186**, 12–19.

38 A. B. Fernández, I. Lezcano-Gonzalez, M. Boronat, T. Blasco and A. Corma, Study of the Beckmann rearrangement of acetophenone oxime over porous solids by means of solid state NMR spectroscopy, *Phys. Chem. Chem. Phys.*, 2009, **11**, 5134–5141.

39 Y. Zhang, L. Qi, A. Lund, P. Lu and A. T. Bell, Mechanism and kinetics of acetone conversion to isobutene over isolated Hf sites grafted to silicalite-1 and SiO$_2$, *J. Am. Chem. Soc.*, 2021, **143**, 8352–8366.

40 L. Botti, S. A. Kondrat, R. Navar, D. Padovan, J. S. Martinez-Espin, S. Meier and C. Hammond, Solvent-activated

This journal is © the Partner Organisations 2022

Inorg. Chem. Front., 2022, **9**, 2395–2402 | **2401**

hafnium-containing zeolites enable selective and continuous glucose–fructose isomerisation, *Angew. Chem., Int. Ed.*, 2020, **59**, 20017–20023.

41 E. Gianotti, M. E. Raimondi, L. Marchese, G. Martra, T. Maschmeyer, J. M. Seddon and S. Coluccia, A spectroscopic study of group IV transition-metal-incorporated direct templated mesoporous catalysts. Part 2. A comparison of Ti-, Zr- and Hf-containing materials, *Catal. Lett.*, 2001, **76**, 21–26.

42 R. L. Oliveira, I. G. Bitencourt and F. B. Passos, Partial oxidation of methane to syngas on Rh/Al$_2$O$_3$ and Rh/Ce-ZrO$_2$ catalysts, *J. Braz. Chem. Soc.*, 2013, **24**, 68–75.

43 Y. V. Larichev, O. V. Netskina, O. V. Komova and V. I. Simagina, Comparative XPS study of Rh/Al$_2$O$_3$ and Rh/TiO$_2$ as catalysts for NaBH$_4$ hydrolysis, *Int. J. Hydrogen Energy*, 2010, **35**, 6501–6507.

44 Y. Lei, J. Jelic, L. C. Nitsche, R. Meyer and J. Miller, Effect of particle size and adsorbates on the L$_3$, L$_2$ and L$_1$ X-ray absorption near edge structure of supported Pt nanoparticles, *Top. Catal.*, 2011, **54**, 334–348.

45 Z. Li, T. He, L. Liu, W. Chen, M. Zhang, G. Wu and P. Chen, Covalent triazine framework supported non-noble metal nanoparticles with superior activity for catalytic hydrolysis of ammonia borane: from mechanistic study to catalyst design, *Chem. Sci.*, 2017, **8**, 781–788.

46 G. Guella, C. Zanchetta, B. Patton and A. Miotello, New insights on the mechanism of palladium-catalyzed hydrolysis of sodium borohydride from ^{11}B NMR measurements, *J. Phys. Chem. B*, 2006, **110**, 17024–17033.

47 Q. Sun, N. Wang, R. Bai, Y. Hui, T. Zhang, D. A. Do, P. Zhang, L. Song, S. Miao and J. Yu, Synergetic effect of ultrasmall metal clusters and zeolites promoting hydrogen generation, *Adv. Sci.*, 2019, **6**, 1802350.

48 N. Wang, Q. Sun, T. Zhang, A. Mayoral, L. Li, X. Zhou, J. Xu, P. Zhang and J. Yu, Impregnating subnanometer metallic nanocatalysts into self-pillared zeolite nanosheets, *J. Am. Chem. Soc.*, 2021, **143**, 6905–6914.